Theory of superconducting wire networks and Josephson-junction arrays in magnetic fields

Qian Niu

Department of Physics, University of California, Santa Barbara, California 93106

Franco Nori

Institute for Theoretical Physics, University of California, Santa Barbara, California 93106

In this paper we study the superconducting-normal phase boundaries of a variety of wire networks and Josephson-junction arrays. We have obtained the mean-field phase diagrams for a number of geometries and compared them to the corresponding experimental data. We have introduced an analytical approach to the analysis of the structures present in the phase diagrams. We have shown in great detail how the gross structure is determined by the statistical distributions of the cell areas, and how the fine structures are determined by correlations among neighboring cells in the lattices. We have also studied the effect of thermal fluctuations on the structure of the phase diagram by a cluster mean-field calculation and a real-space renormalization-group (RG) theory. The RG theory provides a natural link between the structures at fractional fluxes to those at integral ones, predicting a pronounced hierarchical behavior of the phase diagram and an infinite slope for the cusps.

I. INTRODUCTION

Superconducting networks[1] made of thin wires,[2] proximity-effect junctions,[3] and tunnel junctions[4] exhibit interesting forms of phase diagrams when they are immersed in magnetic fields. Various kinds of geometries of such superconducting networks have been studied, including simple[2-4] and complex[5] periodic lattices, regular fractals,[6] bond-percolation networks,[7] disordered arrays[8] and quasiperiodic lattices.[9-14] The rich structure present in the superconducting-normal *phase diagram*, namely the resistive transition temperature as a function of the magnetic field, has been the major concern of several experimental and theoretical[15,16] investigations. Other works[17] have focused on the ground-state configurations and critical currents in Josephson-junction arrays.

The theme of this article is twofold. In the first part, we present an analytical approach to the determination of phase diagrams for a variety of networks and give a rather detailed analysis of the relationship between the phase diagram structure and the corresponding network geometries. In the second part, we study the effect of thermal fluctuations on the structures of the phase diagrams through a cluster mean-field calculation and an approximate renormalization-group theory.

Generally speaking, the rich structure in the phase diagrams is a result of frustration or interference effect due to the magnetic field and the built-in multiple connectedness of the networks. Physical intuition suggests that the basic *cell-fluxes*—the magnetic fluxes through the cells of various areas measured in units of the flux quantum $\Phi_0 \equiv hc/2e$ —are useful parameters to characterize the frustration effect. At zero magnetic field, where the cell fluxes are zero, one expects the frustration effect to be absent, and therefore the resistive transition temperature should have a peak. Also, by a gauge invariance argu-

ment, physical quantities should depend only on the cell fluxes modulo Φ_0. These arguments qualitatively explain the apparent periodic or quasiperiodic structures observed in phase diagrams of networks of various geometries. In fact, the cell fluxes have been used to index the primary peaks of phase diagrams located at particular field values where all the basic cell fluxes become integers or nearly integers.

To have a quantitative description of the phase diagrams, one has to go beyond the mere concept of cell fluxes. Mean-field theory seems to be very effective in serving such a purpose. For wire networks, the mean-field expression is given by the Landau-Ginsburg equation expressed in terms of the order parameters at the nodes.[15] For a junction array, one has a set of self-consistent equations[16] for the thermally averaged pair wave functions of the grains. Such equations are linearized near the transition point, and the highest temperature at which a nontrivial solution first appears is identified as the transition temperature. So one is left to find the top spectral edges of eigenvalue problems. The equations for a junction array can be mapped into a tight-binding Schrödinger problem for an electron hopping on a lattice immersed in a magnetic field. The equations for a wire network are in general more difficult to solve, because the eigenvalue appears in a nonlinear way. Numerical results have been obtained for phase diagrams of networks of various geometries. All of them seem to compare very well with the corresponding experimental data; the locations of the peaks of various sizes are correctly predicted and the relative heights of the peaks are also reproduced with occasional small deviations. The success of mean-field theory suggests that much of the frustration effect in a statistical problem can be accounted for in terms of interference effect of linear wave mechanics.

It is, however, difficult to see through the numerical or

experimental data, exactly how the geometry of a network determines the structure of the phase diagram. There have been attempts to analyze the results of large-scale numerical solutions through those of step-by-step small size calculations.[5,12,15] In this way, one can get a clue as to what extent the gross structure of the phase diagram is determined by the local geometry of a network; but the effect of boundaries often renders one to draw a more precise conclusion. We were thus motivated to propose an analytical approach[12] to the solution of the phase diagrams, based on an explicit step-by-step implementation of the Lanczos method,[18] a well known numerical scheme. In this article, we elaborate on this method. One particular advantageous aspect of this method, which we want to exploit, is that it provides a systematic approximation scheme (through finite truncations) for the spectral edges of eigenvalue problems into which our mean-field phase diagrams translate. The convergence of the approximations to the exact result is usually rapid, and the first few orders work quite well. Furthermore, the first three or four orders of truncations are simple enough to be studied in closed-form analytically, thus enabling us to do a more detailed analysis than before. Furthermore, with the aid of a personal computer, higher orders can be easily studied, and there is no difficulty in seeing the general trend. As can be seen from the subsequent sections, our approach can provide considerable theoretical insight into the physical origin of the structure in the phase diagrams. Geometric factors of a network, such as the statistics of single-cell areas and the correlation of two or more neighboring cell areas, enter successively into the truncated Lanczos Hamiltonians order by order. From this fact and the manner that different truncations give different approximations of the phase diagram, we can conclude that the gross structure in the phase diagram is simply a result of single-cell statistics, and secondary and higher order structures are due to certain correlation of neighboring cells, and so on.

In Sec. II we give a brief description of the mean-field theory and a general formulation of the Lanczos method on which our approach is based. In Sec. III we study networks which are periodic in one direction. Several periodic, quasiperiodic and random lattices in this category are studied in detail, and the results are compared with experimental data. In Sec. IV we formulate our approach for general geometries, and give a detailed study of a few special cases for demonstration.

With regards to the validity of the mean-field theory, there has been some confusion and controversy. Our analytical approach, of course, does not resolve them, for it is within the framework of mean-field theory. We devote Sec. V to a discussion of this problem, and particularly the effect of thermal fluctuations on the structure of the phase diagrams. We will derive a cluster mean-field theory and an approximate renormalization group theory for the phase diagram of a square lattice of Josephson junctions. The renormalization group approach is interesting in its own right, for it relates the fractional fluxes to the integral ones, giving account for the self-similarity of the phase diagram. It also predicts an infinite slope for the peaks in the phase diagram, which

might be checked in a very accurate experimental measurement. The last section summarizes our results.

II. MEAN-FIELD THEORY AND THE LANCZOS APPROACH

In this section we present a brief derivation of the mean-field equations for superconducting networks and give a general formulation of our analytical approach for the solution of the phase diagrams. The main purpose of doing so is to provide a general theoretical framework for subsequent investigations. We will also reduce, following Alexander,[15] the nonlinear eigenvalue problem for wire networks to a linear one. As shown below, such reduction can greatly simplify the numerical calculations for wire networks and the application of the Lanczos method on such systems.

Consider first a Josephson-junction array, i.e., an array of superconducting grains coupled together through the Josephson effect. Below the transition temperature T_{c0} of the superconducting material, the individual grains have acquired a superconducting order parameter whose magnitude is finite and relatively fixed, but whose phase may fluctuate more or less independently from grain to grain, such that the whole system may still be in a nonsuperconducting state. Only at a sufficiently lower temperature T_c, phase coherence can be established throughout the system. This is driven by the Josephson effect. In the simplest form, the Josephson coupling energy between a pair of neighboring grains is

$$-J_{ij}\cos(\theta_i - \theta_j) \, , \qquad (2.1)$$

where $J_{ij} > 0$ is a constant setting the energy scale and θ_i is the phase of the order parameter of the ith grain. In the presence of a magnetic field, (2.1) is modified to the following form:

$$-J_{ij}\cos(\theta_i - \theta_j - A_{ij}) \, , \qquad (2.2)$$

where $A_{ij} = \int \mathbf{A} \cdot d\mathbf{l}$ is the line integral of the vector potential from the center of grain i to j, if we ignore (we will do so throughout the paper) a constant factor which is 2π divided by the flux quantum $hc/2e$. The canonical partition function then is

$$Z = \sum_{\{\theta\}} \exp\left[\sum_{\langle ij \rangle} \frac{J_{ij}}{kT}\cos(\theta_i - \theta_j - A_{ij})\right] \, , \qquad (2.3)$$

from which all thermodynamic properties can be derived at least in principle. Shi and Stroud[16] derived a set of mean-field equations for the thermally averaged local phase factors $\langle e^{i\theta_j} \rangle \equiv \psi_j$, whose linearization near $\psi_j \approx 0$ has the following form:

$$2kT\psi_i = \sum_j J_{ij} e^{iA_{ij}}\psi_j \, , \qquad (2.4)$$

where the summation is over the nearest neighbors only. The superconducting transition temperature is identified as the highest temperature at which a nontrivial solution first appears.

Consider now a superconducting wire network. Fol-

lowing the original ideas of De Gennes and Alexander,[15] one takes the linearized Landau-Ginsburg equation as the starting point, and expresses everything (by integrating the equation along the wire segments) in terms of the order parameters at the nodes. The current conservation condition then relates the order parameter ψ_i, at node i, to those at its nearest-neighboring nodes j as

$$-\psi_i \sum_j \cot\left[\frac{l_{ij}}{\xi}\right] + \sum_j \frac{\psi_j e^{iA_{ij}}}{\sin(l_{ij}/\xi)} = 0 , \qquad (2.5)$$

where l_{ij} is the distance between nodes i and j, and the parameter ξ is the coherence length depending on temperature in the following way

$$\xi(T) = \xi_0 \left[\frac{T_0}{T_0 - T}\right]^{1/2} , \qquad (2.6)$$

with T_0 as the transition temperature at zero field. Again, the transition temperature at general field value is given by the highest temperature at which a nontrivial solution of (2.5) appears. In general, Eq. (2.5) is difficult to solve, for the eigenvalue parameter ξ appears in a nonlinear way. However, if all the lengths are the same ($l_{ij} = l$), the equation can be reduced to

$$\cos\left[\frac{l}{\xi}\right]\phi_i = \sum_j e^{iA_{ij}}(z_i z_j)^{-1/2}\phi_j , \qquad (2.7)$$

which is a standard eigenvalue problem with an eigenvalue parameter $\cos(l/\xi)$, where $\phi_i \equiv (z_i)^{1/2}\psi_i$, and z_i is the coordination number of node i. In general cases where l_{ij} are not all the same, exact reduction cannot be found. However, if the lengths are not very different, we expect $l_{ij}/\xi \ll 1$ for the critical coherence length. An approximation based on this estimate reduces (2.5) to the following form:

$$-\frac{l^2}{2\xi^2}\phi_i = \sum_j \left[\frac{l}{l_{ij}}(\alpha_i\alpha_j)^{-1/2}e^{iA_{ij}}\phi_j\right]$$
$$- \left[\sum_j \frac{l}{l_{ij}}\right]\alpha_i^{-1}\phi_i , \qquad (2.8)$$

where $\alpha_i \equiv \sum_j l_{ij}/l$, $\phi_i \equiv \alpha_i^{1/2}\psi_i$, and l is a typical scale of l_{ij} used simply to make the parameters dimensionless. A detailed justification of the approximation is given in Appendix A, where one can see that it works well even for a lattice of quite different lengths of wire segments. Again, we have arrived at a standard eigenvalue equation with an effective energy parameter $-l^2/2\xi^2$. Efficient algorithms can be used for relatively large scale numerical calculations.

Now we are ready to discuss the Lanczos method.[18] Observe that all we need in solving Eqs. (2.4) or (2.8) is to find the top spectral edge which is proportional to the transition temperature. It is well known that the Lanczos method is particularly good at locating spectral edges. The following defines the basics of the method.

Let H be the Hamiltonian matrix in our eigenvalue problem. Choose an initial state ψ_1, and do the following expansion

$$H\psi_1 = \beta_1\psi_1 + \psi_2 ,$$
$$H\psi_2 = \gamma_2\psi_1 + \beta_2\psi_2 + \psi_3 ,$$
$$H\psi_3 = \gamma_3\psi_2 + \beta_3\psi_3 + \psi_4 , \qquad (2.9)$$
$$H\psi_4 = \gamma_4\psi_3 + \beta_4\psi_4 + \psi_5, \cdots ,$$

where each new state is required to be orthogonal to the previous ones. As one can verify, this requirement uniquely defines all the parameters $\{\beta_i, \gamma_i\}$ in the expansion. The H matrix in the basis $\{\psi_i\}$ is obviously in a tridiagonal form, and moreover it can be put into a real symmetric form if we use the normalized states

$$\tilde{\psi}_i = \gamma_i^{-1/2}\psi_i \qquad (2.10)$$

as a basis.

Of course, the expansion is useful only if finite truncations give good approximation to the quantities we desire, i.e., the top spectral edge (denoted as ε_t). A theorem tells us that if the initial ψ_1 has a finite overlap with the state ψ_t at ε_t, then the top eigenvalue ε_n of the sub-Hamiltonian H_n, spanned by $\{\psi_1, \ldots, \psi_n\}$, converges to ε_t monotonically. The convergence will be fast if ψ_1 is reasonably close to ψ_t.

III. NETWORKS PERIODIC IN ONE DIRECTION

In this section we use the Lanczos method to study 2D superconducting networks which are periodic in one direction. More specifically, we assume the networks to have a structure of a rectangular lattice with uniform lattice spacings in the y direction and variable spacings in the x direction (strip-type geometries). The mean-field equations (2.8) for a wire network can be readily reduced to a one-dimensional form

$$-\frac{l^2}{2\xi^2}\phi_n = \left[2\cos(Blx_n + q) - \left[2 + \frac{l}{l_n} + \frac{l}{l_{n+1}}\right]\right]\alpha_n^{-1}\phi_n$$
$$+ \frac{l}{l_{n+1}}(\alpha_n\alpha_{n+1})^{-1/2}\phi_{n+1}$$
$$+ \frac{l}{l_n}(\alpha_n\alpha_{n-1})^{-1/2}\phi_{n-1} ,$$

$$(3.1)$$

where $\alpha_n = 2 + (l_n + l_{n+1})/l$, $l_n = x_n - x_{n-1}$, and x_n is the x coordinate of the lattice point (n, m). In the derivation of the above equations we have taken the gauge $A = (0, Bx)$ and written ϕ_{nm} as $\phi_n e^{iqm}$. At this stage, we would like to remind the reader that we have taken $2\pi/\Phi_0$ as the unit of the magnetic field B, where Φ_0 is the flux quantum. In a similar fashion, the mean-field Eq. (2.4) for a Josephson-junction array can be reduced to a one-dimensional form

$$2kT\phi_n = J_n^x 2\cos(Blx_n + q)\phi_n$$
$$+ J_{n+1}^y\phi_{n+1} + J_n^y\phi_{n-1} , \qquad (3.2)$$

where the J's are the coupling constants.

An important observation is that in (3.1) and (3.2) the neighboring couplings are all positive. This implies that

the state at the top spectral edge can be taken as positive everywhere. This fact immediately suggests that we can take the uniform state (ϕ_n independent of n) as a reasonably good starting state, ψ_1, in the Lanczos method [see the remarks below (2.9)]. From here on, we will concentrate our attention to Eq. (3.2) with all the coupling constants the same (say, $=1$). This will simplify the notation considerably while still keep the essential physics (frustration effect, for instance) in Eqs. (3.1) and (3.2). All the geometrical information of the superconducting network will then be contained in the sequence $\{x_n\}$. For the cases studied below, the top spectral edge is actually realized at $q=0$, so we will set $q=0$.

With a uniform starting state (with amplitude $=1$ everywhere), the Lanczos method generates the following set of parameters [defined in Eq. (2.9)]

$$\beta_1 = 2, \quad \gamma_2 = 2 ,$$

$$\beta_2 = 2 \langle \cos(BS_n) \rangle, \quad \gamma_3 = 3 - \beta_2^2 + 2 \langle \cos B (S_n + S_{n+1}) \rangle ,$$

$$\beta_3 = \frac{1}{\gamma_3} [\beta_2^3 - \beta_2 - 2\beta_2(\gamma_3 - 3 + \beta_2^2) \tag{3.3}$$

$$+ 2 \langle \cos 2B (S_n + S_{n+1}) \rangle$$

$$+ 2 \langle \cos B (S_n + S_{n+1} + S_{n+2}) \rangle], \quad \cdots ,$$

where $\langle \ \rangle$ denotes an average over n, and $S_n \equiv ll_n$ is the cell area. Given any sequence of cell areas, the averages can be easily computed.

In the following, we present a detailed analysis of the phase diagrams for five examples of the network geometry. These examples are representative of periodic, quasiperiodic and random lattices. The roles played by different area ratios of the cells, the population ratios of different cells and their geometrical arrangements are explored. For completeness, the results of large-size mean-field calculations are also displayed, and they are compared with the experimental phase diagrams obtained by Behrooz et al.[9] However, readers should be warned that the experimental data were obtained for wire networks, while our theoretical results for strip-type geometries are, strictly speaking, for Josephson junction arrays. Nevertheless, since the two types of superconducting networks are governed by similar physical laws, at least at the level of mean-field theory as can be seen from Eqs. (3.1) and (3.2), they should exhibit similar features in the phase diagrams. Indeed, as can be seen from below, the comparison between theory and experiment is reasonably good in general and very good with regards to the location of the cusps. Some deviations between the two will be commented upon at the very end of this section.

Example 1. Let us start with the easiest case: a periodic square lattice, i.e., $S_n = a$. We have analytic expressions for the Lanczos parameter of *all* orders,

$$\beta_n = 2 \cos(n-1)Ba ,$$

$$\gamma_n = \begin{cases} 2 & \text{if } n = 2 , \\ 1 & \text{if } n > 2 . \end{cases} \tag{3.4}$$

Note that this system is symmetric about the origin. The Lanczos Hamiltonian obtained this way acts only on the

states with this symmetry. The natural exploitation of the symmetry of the system is another advantage of the Lanczos method.

Figure 1(a) shows the reduced resistive transition temperature, $\Delta T_c(\Phi) = T_c(0) - T_c(\Phi)$, as a function of the magnetic flux, Φ, through a unit cell. Each curve has been computed from Eq. (2.9) with the parameters given by Eqs. (3.3) and (3.4). The highest curve corresponds to the second order expression of the Lanczos Hamiltonian

$$\begin{bmatrix} 2 & 1 \\ 2 & 2\cos(Ba) \end{bmatrix} .$$

It already exhibits correctly the general trend as well as the periodicity of the phase diagram. However, no fine structure is present at this stage. The next lower curve corresponds to the third-order expression

$$\begin{bmatrix} 2 & 1 & 0 \\ 2 & 2\cos(Ba) & 1 \\ 0 & 1 & 2\cos(2Ba) \end{bmatrix} .$$

It has a local minimum corresponding to a half-flux quantum per plaquette and no further fine structure. To understand this, note that in this order of approximation, the geometrical information about the individual cell area as well as the correlation between nearest-neighboring cells are included through the matrix elements $\cos(Ba)$ and $\cos(2Ba)$. The next higher-order expression (fourth order) also includes a $\cos(3Ba)$ matrix element which accounts for the developing structure at $\Phi_0/3$ and $2\Phi_0/3$ in the third curve from the top. Physically speaking, the $\cos(3Ba)$ term manifests the correlation among three neighboring cells. The lowest three curves correspond to the 5th, 10th, and 50th order truncations respectively. The 50th order truncation includes a weighted contribution from many harmonics, from $\cos(Ba)$ to $\cos(50Ba)$, and it gives an excellent approximation to the infinite order case. The convergence is monotonic and fast. More importantly, through the study of different approximations, we can easily identify the physical origin of the structures of various sizes in the phase diagram; as we increase the order of truncation, more and more geometrical information of the lattice is included in the treatment, and finer structures appear and develop [see Fig. 1(b) for details]. [The curves in the inset of Fig. 1(a) will be discussed in the next section. They are plotted here for easier comparison.]

Example 2. A periodic network with a unit cell of two plaquettes with areas a and b, i.e., $S_{2n} = a$, $S_{2n+1} = b$. We have

$$F_1(B) \equiv \langle \cos(BS_n) \rangle = \tfrac{1}{2}[\cos(Ba) + \cos(Bb)] ,$$

$$F_2(B) \equiv \langle \cos[B(S_n + S_{n+1})] \rangle = \cos[B(a+b)] ,$$

$$F_3(B) \equiv \langle \cos[B(S_n + S_{n+1} + S_{n+2})] \rangle \tag{3.5}$$

$$= \tfrac{1}{2} \{ \cos[B(2a+b)] + \cos[B(2b+a)] \} .$$

Figure 2 shows the superconducting-normal phase boundary for the case $a/b = \tau = (1+\sqrt{5})/2$. Figure 2(a) compares experimental measurements[9] with results com-
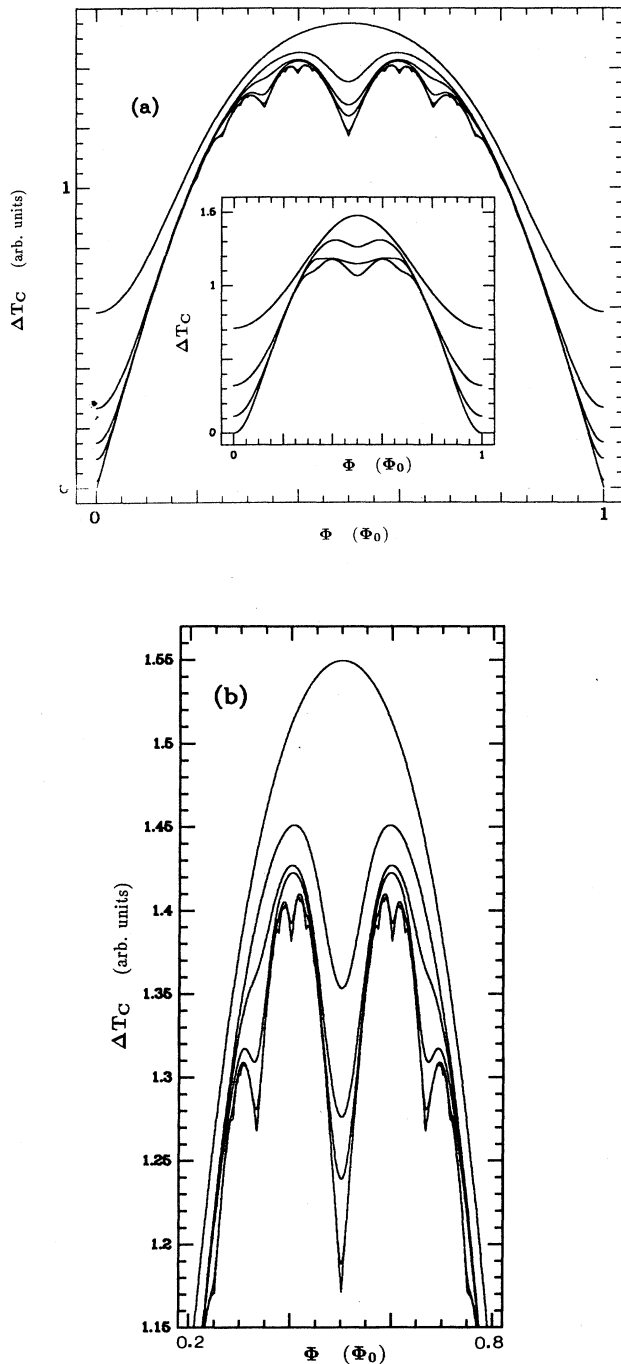
FIG. 1. (a) shows the superconducting transition temperature, $\Delta T_c = T_c(0) - T_c(\Phi)$, for a square lattice, vs the magnetic flux, Φ through a unit cell, computed from the Lanczos Hamiltonian (2.9) and the matrix elements (3.4). From top to bottom, the orders of truncation are 2, 3, 4, 5, 10, and 50. Note the development of fine structures. The convergence is monotonic and fast. *Inset*: same as above but with a strictly localized starting state, instead of an extended (uniform) one. The orders of truncation are 3 (top curve), 4, 5, and 6. The convergence is still monotonic, but slower. In (b), the curves shown in (a) are expanded for easier observation of the fine structures.

puted from the linearized mean-field Eq. (2.7). The agreement between the theoretical and experimental results is good. The same phase boundary computed from Eqs. (3.3) and (3.5) with second- and third-order truncations of the Lanczos Hamiltonian are shown in Fig. 2(b). The main structure of the phase diagram is already correctly shown in the result of 2×2 truncation, and finer structures appear in the result of 3×3 truncation. Note that, in the second order, the Lanczos Hamiltonian depends on terms such as $\cos(Ba)$ and $\cos(2Bb)$ with incommensurate periods, which explains why the phase diagram is nonperiodic even though the lattice itself is periodic. Furthermore, these terms are weighted by the concentrations of the corresponding cell areas, having correctly predicted the relative heights of the main dips and peaks as well as their locations. This suggests that a knowledge of the distribution of cell areas determines the gross structure of the phase diagram. Now, in the third-order approximation, geometrical information such as the joint distribution of two- or three-neighboring cell areas are included through terms of $\cos[B(a+b)]$, $\cos[B(2a+b)]$, $\cos[B(a+2b)]$ as well as their weights. Such information is responsible for the fine structures appeared in the result of 3×3 truncation. More discussion on these points will be given in the next two examples.

Example 3. Fibonacci lattice, $\{S_n\}$ is a Fibonacci sequence of two areas a and b.

$$F_1(B) = \frac{1}{\tau}\cos(Ba) + \frac{1}{\tau^2}\cos(Bb) ,$$

$$F_2(B) = \frac{2}{\tau^2}[B(a+b)] + \frac{1}{\tau^3}\cos(B2a) , \qquad (3.6)$$

$$F_3(B) = \left[\frac{1}{\tau} + \frac{1}{\tau^3}\right]\cos[B(2a+b)] + \frac{1}{\tau^4}\cos[B(2b+a)] ,$$

where $\tau = (\sqrt{5}+1)/2$. In fact, there is a closed form ex-
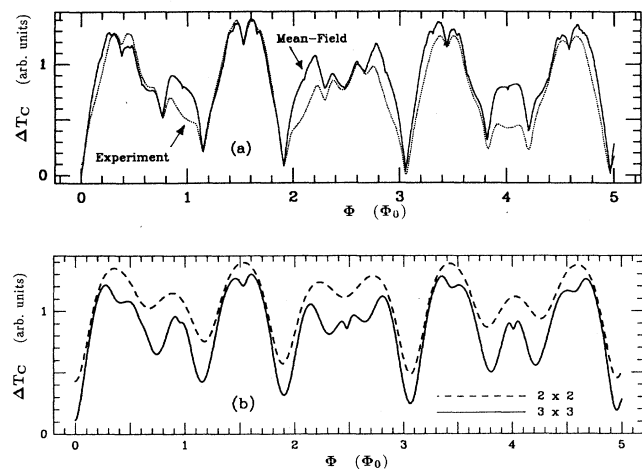
FIG. 2. Resistive transition temperature, $\Delta T_c = T_c(0) - T_c(\phi)$, vs magnetic flux through a big cell for a periodic lattice with a unit cell containing two plaquettes of area ratio τ: (a) experimental data for a wire network (Ref. 9) and the mean field result (continuous line); (b) second- and third-order approximations to ΔT_c.

pression for the distribution of the sum, L_N, of N consecutive areas in the sequence. For a given N, there are only two possibilities

$$L_N = \left[\frac{N}{\tau}\right]a + \left\{N - \left[\frac{N}{\tau}\right]\right\}b ,$$

and

$$L_N = \left\{\left[\frac{N}{\tau}\right] + 1\right\}a + \left\{N - 1 - \left[\frac{N}{\tau}\right]\right\}b ,$$

with probabilities $1 - \{N/\tau\}$ and $\{N/\tau\}$, respectively, where $[x]$ and $\{x\}$ denote the integer and fractional parts

of x. The above result can be proved by using the circle map construction of the Fibonacci sequence.[19]

Three cases in this example are studied in detail, with area ratios equal to (i) τ, (ii) $7^{1/3}$, and (iii) 2.

(i) $a/b = \tau$. In Fig. 3(a), the experimental phase diagram[9] is compared with the result of a large size mean-field calculation. The correspondence is again quite close. The same phase diagram computed from the first few truncations of the Lanczos Hamiltonian is shown by the curves in Fig. 3(b). The locations as well as the relative heights of the main dips and peaks are correctly reproduced in the second-order approximation. To this order, only the statistical distribution of single-cell areas is involved. Some fine structures emerge in the third-
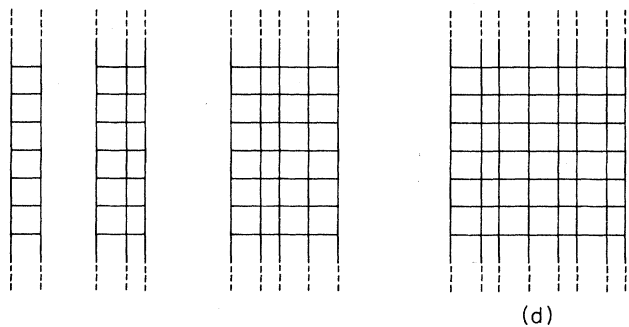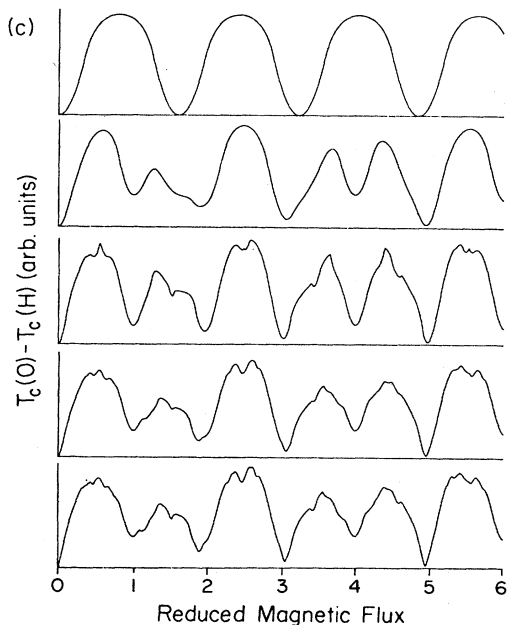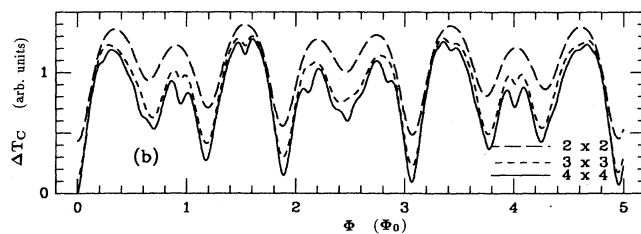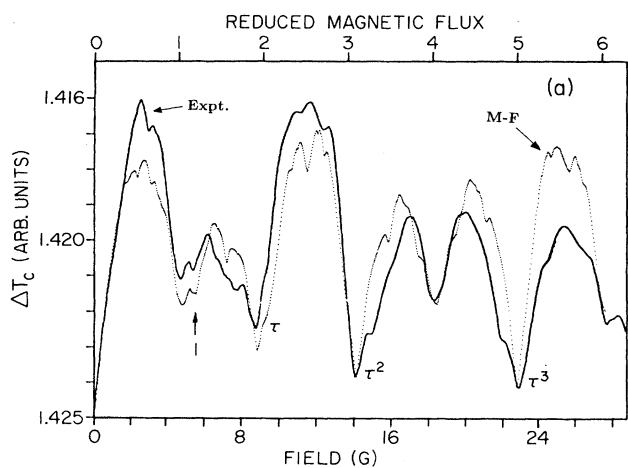
FIG. 3. Superconducting transition temperature, ΔT_c, vs magnetic flux per large cell for a 2D Fibonacci lattice of area ratio τ: (a) the experimental data for a wire network (Ref. 9), and the mean-field result (dotted line); (b) second-, third-, and fourth- (from top to bottom) order approximations to $\Delta T_c(\Phi)$; (c) mean-field results for finite portions of the Fibonacci lattice with 500 equidistance horizontal lines and 2, (top curve), 3, 5, 8, 13 vertical lines, respectively; (d) examples of strip-type geometries with 2, 3, 5, and 8 vertical lines, respectively.

order approximation, which includes the joint distributions of two-and three-neighboring cell areas. Additional finer structures appear in the fourth-order approximation, which also includes the joint distributions of four- and five-neighboring cell areas. This way, we can identify what kind of geometrical information is responsible for the structures of various sizes in the phase diagram.

This issue has also been explored by finite-size studies. We have numerically solved the mean field equation for lattices of different sizes and observed the pattern evolution of the phase diagram as a function of system size. Figure 3(c) shows such calculation for lattices with strip-type geometry [see Fig. 3(d)], i.e., 500 equidistant vertical lines and 2 (top curve), 3,5,13 (bottom curve) horizontal lines, respectively. From this result, it becomes clearer how short-range correlations among neighboring cells are responsible for the overall structure of the phase boundary and how longer-range correlations are responsible for the finer structures and, in particular, of sharper downward cusps. Upward cusps in small networks are due to level crossings and not to long range correlations among cells.[5]

(ii) $a/b = 7^{1/3}$. Unlike the previous case, the area ratio is different from the population ratio of the two areas. In Fig. 4(a) the experimental data[9] is compared with the result of a large size mean-field calculation. The correspondence is quite close. The same phase diagram computed from the first few approximants of the Lanczos Hamiltonian is shown by the curves in Fig. 4(b). Remarkably, the general trend and main structure of the phase diagram is controlled by the second approximants of the Lanczos Hamiltonian through the terms, $\cos(Ba)$ and $\cos(Bb)$, weighted by the concentrations of the corresponding cell areas in the lattice. As more geometrical information is included in the treatment by increasing the order of truncation, finer structures appear and develop.
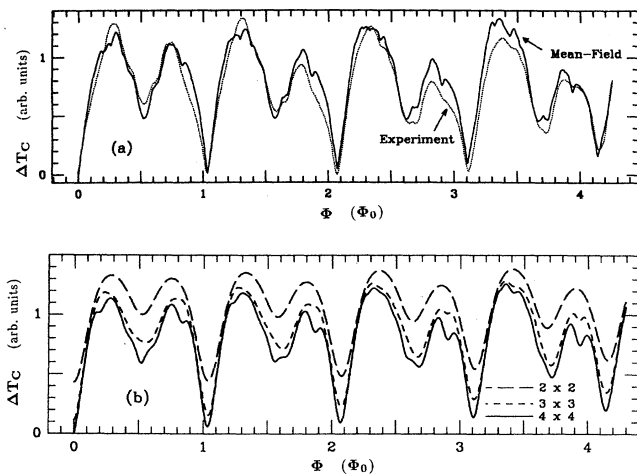
(iii) $a/b = 2$. This is a case of commensurate area ratio. The experimental phase diagram[9] and a numerical mean field result are shown in Fig. 5(a). The correspondence is very good. The periodicity and the reflectional symmetry of the phase diagram can be easily understood through the Lanczos Hamiltonian, whose matrix elements are periodic in the magnetic field and are symmetric about zero and half-flux quantum through the bigger cell. The quasiperiodicity of the lattice has *no* effect on this behavior. Through the first few approximations of the phase diagram, as shown in Fig. 5(b), we can follow the evolution of the structural pattern. The fine structures at $\frac{1}{5}$, $\frac{2}{5}$ cell fluxes (and their equivalents) in the fourth-order approximation indicate the occurrence of phase coherence over the cell-cluster configuration, a-b-a.

Example 4. Random distribution of two areas a and b with concentrations $1/\tau$ and $1/\tau^2$, respectively:

$$F_1(B) = \frac{1}{\tau}\cos(Ba) + \frac{1}{\tau^2}\cos(Bb) ,$$

$$F_2(B) = \frac{2}{\tau^3}\cos[B(a+b)] + \frac{1}{\tau^2}\cos(B2a) + \frac{1}{\tau^4}\cos(B2b) ,$$

$$\tag{3.7}$$

$$F_3(B) = \frac{1}{\tau^3}\cos(B3a) + \frac{3}{\tau^4}\cos[B(2a+b)]$$

$$+ \frac{3}{\tau^5}\cos[B(a+2b)] + \frac{1}{\tau^6}\cos(B3b) .$$

In Fig. 6(a), the experimental phase diagram is compared with the result of a large size numerical calculation of the mean-field theory. Although the overall trend of the two curves agree with each other, some of the fine structures predicted by the theory are not observed in the experimental data. The results of second- and third-order approximations are shown in Fig. 6(b). In the second order, the Lanczos matrix is identical to that of the first case of example 3, for it only depends on the dis-

FIG. 4. Resistive transition temperature vs magnetic flux per large cell for a Fibonacci lattice with an area ratio of $7^{1/3}$: (a) the experimental data[9] for a wire network (Ref. 9), and our mean-field results (solid line); (b) second-, third-, and fourth-order approximations to $\Delta T_c(\Phi)$.
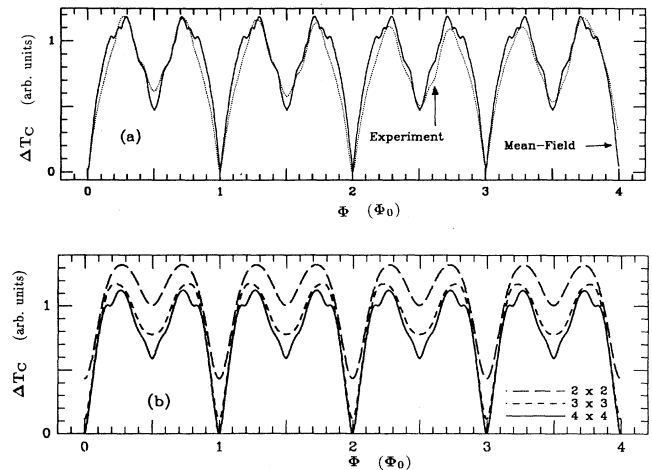
FIG. 5. ΔT_c vs magnetic flux per small cell for a Fibonacci network with an area ratio of 2: (a) experimental data on a wire network (Ref. 9) and the mean-field result (solid line); (b) second-, third-, and fourth-order approximations to $\Delta T_c(\Phi)$.

tribution of single-cell areas. This explains why the gross structures for the random and nonrandom Fibonacci lattices are the same. However the fine structures in the third order approximations are less pronounced than those for the nonrandom case. This difference comes from the fact that the distribution of neighboring cell areas is different in the two cases. We also considered several samples of finite random Fibonacci lattices and compared their respective phase boundaries [see Fig 6(c)]. The result supports the idea that a controlled degree of "randomness" in the geometrical arrangement of the cells (here we are not referring to randomness in their areas) tends to wash out the fine structures but not the gross one.

Example 5. Superposition of two incommensurate periodic (TIP) sequences. In this case, $\{x_n\} = \{a(n_1 + \gamma n_2)\}$ rearranged in increasing order, where n_1 and n_2 run through the integers, and γ is an irrational number. For example, for $\gamma = \tau$ (the golden mean), we have

$$\ldots, \quad x_{-2} = -a, \quad x_{-1} = 0a, \quad x_0 = 0\tau a, \quad x_1 = a ,$$

$$x_2 = \tau a, \quad x_3 = 2a, \quad x_4 = =3a , \ldots .$$

We have derived a general formula for the distribution of the sum, L_N, of N consecutive spacings in this sequence. First, L_N is uniformly distributed in the interval
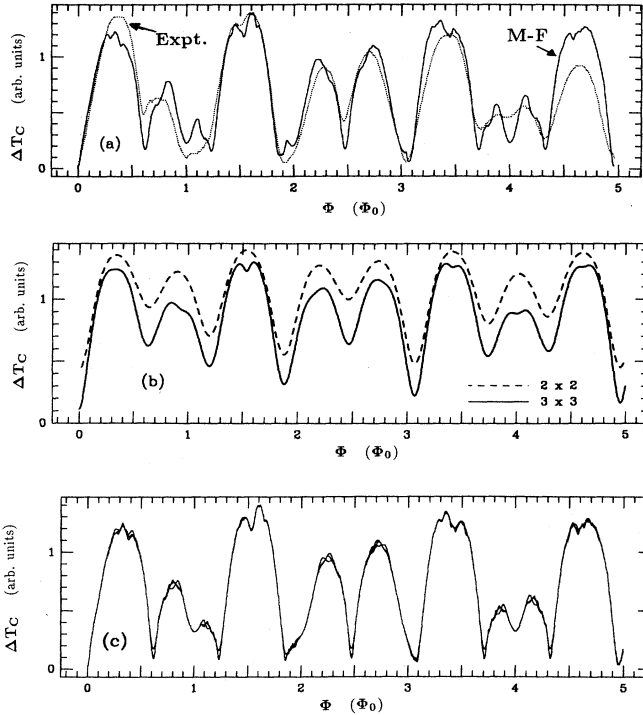
FIG. 6. Superconducting transition temperature, ΔT_c vs magnetic flux per large cell for the random Fibonacci lattice of area ratio τ: (a) experimental data for a wire network (Ref. 9) and our mean-field result (solid line); (b) second-, and third-order approximations to $\Delta T_c(\Phi)$; (c) mean-field result for three random Fibonacci lattices generated with different seeds.

(x_{N-1}, x_N), with total probability equal to

$$\frac{2}{\alpha(\gamma + 1)}(x_N - x_{N-1}) .$$

Second, the distribution has two δ function peaks at the boundaries of this interval, with probabilities

$$\mathcal{P}\{L_N = x_N\} = \frac{1}{a(\gamma + 1)}(y_{N+1} - x_N) ,$$

$$\mathcal{P}\{L_N = x_{N-1}\} = \frac{1}{a(\gamma + 1)}(x_{N-1} - z_{N-2}) ,$$

where y_{N+1} (z_{N-2}) is the next site above x_N (below x_{N-1}) which belongs to a different subsequence than $x_N(x_{N-1})$. Applying these formulas to the special case of $\gamma = \tau$, we obtain

$$P(L_1) = \frac{2}{\tau^2}\chi(L_1; 0, a) + \frac{1}{\tau^3}\delta(L_1 - a) ,$$

$$P(L_2) = \frac{1}{\tau^2}\delta(L_2 - a) + \frac{2}{\tau^3}\chi(L_2; a, \tau a) + \frac{1}{\tau^4}\delta(L_2 - \tau a) ,$$

$$P(L_3) = \frac{1}{\tau^3}\delta(L_3 - \tau a) + \frac{2}{\tau^4}\chi(L_3; \tau a, 2a) + \frac{2}{\tau^3}\delta(L_3 - 2a) ,$$

where $\chi(x; x_1, x_2) = 1/(x_2 - x_1)$, if $x_1 \le x \le x_2$, and equal to zero otherwise. We then have for the averages

$$F_1(B) = \frac{1}{\tau^3}\cos(Ba) + \frac{2}{\tau^2 Ba}\sin(Ba) ,$$

$$F_2(B) = \frac{1}{\tau^2}\cos(Ba) + \frac{1}{\tau^4}\cos(B\tau a)$$

$$+ \frac{2}{\tau^2 Ba}[\sin(B\tau a) - \sin(Ba)] , \qquad (3.8)$$

$$F_3(B) = \frac{1}{\tau^3}\cos(B\tau a) + \frac{2}{\tau^3}\cos(B2a)$$

$$+ \frac{2}{\tau^2 Ba}[\sin(B2a) - \sin(B\tau a)] .$$

Figure 7(a) shows the phase diagram obtained from the first few truncations of the Lanczos Hamiltonian. The general feature is rather well produced by the 2×2 truncation; there is a deep dip at the origin and shallower dips at near-integral values of the reduced flux $\phi \equiv Ba/2\pi$. The rising up of the dips away from the origin is due to the destructive interference effect from the continuous distribution of the areas, as can be seen from the second term of $F_1(B)$, which falls off inversely with the field. Finer structures show up in the results of 3×3 and 4×4 truncations, which corresponds to the new periods in $F_2(B)$ and $F_3(B)$ coming from the distributions of L_2 and L_3. There is not much difference between the result of 4×4 truncation and that of a large size mean-field calculation. Figure 7(b) compares the full mean-field result with the experimental data. The correspondence is not satisfactory, although the gross structure agrees. We will comment on this at the end of this section.

In summary, through the detailed studies of these examples, we can draw the following conclusion regarding the structures in the phase diagrams and their relationship to the geometries of the superconducting networks.
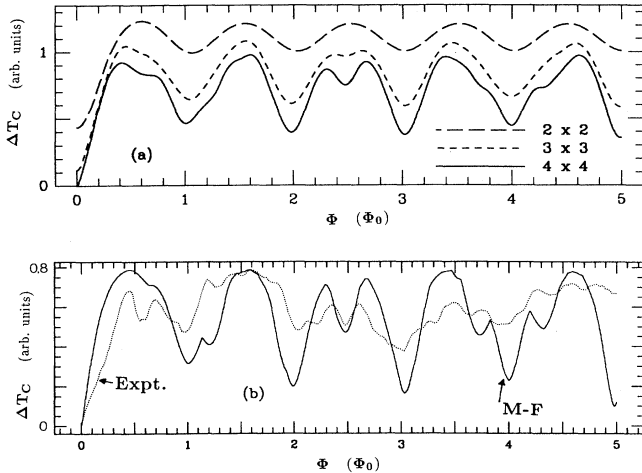
FIG. 7. ΔT_c vs magnetic flux per small period for the lattice of TIP with period ratio τ (see the text for its description): (a) second-, third-, and fourth-order approximations to $\Delta T_c(\Phi)$; (b) experimental data for a wire network (Ref. 9) and the mean-field result (solid line).

The general trend and the gross structure are rather well predicted by the second approximant of the Lanczos treatment, which only depends on the statistical distributions of single-cell areas, disregarding their geometrical arrangement. Some fine structures appear in the third-order approximation, which also depends on the distributions of two- and three-neighboring cells. Additional finer structures emerge and develop in the fourth- and higher-order approximations, which depend on the distributions of even larger clusters of neighboring cells. It is therefore clear that the structures of various sizes in the phase diagram have their physical origins from the geometrical properties of the networks. Such a correspondence is made precise by our systematic analysis using the Lanczos method.

Finally, we would like to comment on the discrepancies between our results and the experiments of Behrooz et al.[9] At first, the deviations might be attributed to the fact that the experiments were done on wire networks while our strip geometry results discussed in the previous examples are, strictly speaking, for Josephson-junction arrays. Our primary study shows that this is clearly not the case. The phase diagrams computed from the wire network Eqs. (2.5) or (3.1) give no better agreement with the experiments. It has been pointed out by the authors of Ref. 9 that the deviations are more likely due to the imperfections in the experimental samples, especially for the TIP network in example 5.

IV. NETWORKS OF GENERAL GEOMETRY

Without translational symmetry there is no simple way to transform the mean-field equations to problems with positive couplings everywhere. Therefore it is not clear

what kind of starting state should be chosen to generate the Lanczos Hamiltonian such that the lower-order truncations can produce reasonably good approximations to the phase diagram. Besides, if we insist on using a uniform state as the starting state, hoping that there might be a particular gauge of the vector potential in which we can get a good approximation, then we will be facing the new problem of finding that particular gauge. This is even more difficult than solving the original mean field equation.

Let us take a less ambitious stand point. Instead of taking an extended starting state, we choose a strictly localized state to generate the Lanczos Hamiltonian, and see what we can get this way. This is partly motivated by our general understanding of the locality properties of wave mechanics and partly inspired by the success of finite-size numerical calculations for extended systems. From the structure of (2.4) or (2.8), each new state in the Lanczos method expands outward by one more step from the site where the starting state is located. Thus an nth order truncation can cover a region of radius n of the network. This should be compared with finite size calculations for which one has to deal with a matrix of n^2th order in order to cover the same region in two dimensions. Furthermore, the parameters in the Lanczos Hamiltonian are gauge invariant quantities, because our starting state is gauge invariant except for a phase factor which never enter the Lanczos Hamiltonian. Any choice of a fixed starting state other than a one-site state will produce a gauge dependent Hamiltonian. In general, a Lanczos Hamiltonian is only covariant with the starting state according to the rule of gauge transformation, but is not invariant.

Another advantage of using a one-site starting state is that we can have a simple geometric representation of the Lanczos parameters. It can be easily seen from Eq. (2.9) that a knowledge of the first $2n-1$ moments

$$\{ m_k \equiv \langle \psi_1 | H^k | \psi_1 \rangle, \quad k=1,\ldots,n \} \tag{4.1}$$

will be sufficient to build up the nth order truncation of the Lanczos Hamiltonian. For a Josephson-junction array as described by Eq. (2.4), the *geometric significance* of m_n is clear: it is the sum of contributions from all the closed paths of n steps starting and ending at s (the location of the starting state), each with a phase factor of $e^{i\phi_P}$ where ϕ_P is the flux enclosed by the path P. The phase factors describe, in a gauge invariant way, the interference effect of the magnetic field on the transition temperature and they are the source of the rich structures in the phase diagram.

Consider Eq. (3.2) with unity coupling constants. The Lanczos parameters, as defined in Eq. (2.9), can be computed from the moments of the Hamiltonian using the following set of equations recursively

$$\gamma_1 = 0, \quad \beta_1 = 0 ,$$
$$\gamma_n = U_n / U_{n-1}, \quad \beta_n = V_n / U_n, \quad n \geq 2 , \tag{4.2a}$$

where

$$U_1 = 1 ,$$

$$U_2 = m_2 , \quad V_2 = m_3 ,$$

$$U_3 = m_4 - A_{31} m_3 - A_{32} m_2 , \quad V_3 = m_5 - A_{31} m_4 - A_{32} m_3 - A_{31} U_3 , \tag{4.2b}$$

$$U_4 = m_6 - A_{41} m_5 - A_{42} m_4 - A_{43} m_3 , \quad V_4 = m_7 - A_{41} m_6 - A_{42} m_5 - A_{43} m_4 - A_{41} U_4 ,$$

$$U_5 = m_8 - A_{51} m_7 - A_{52} m_6 - A_{53} m_5 - A_{54} m_4 , \quad V_5 = m_9 - A_{51} m_8 - A_{52} m_7 - A_{53} m_6 - A_{54} m_5 - A_{51} U_5 , \ldots ,$$

with the A's given by

$$A_{31} = \beta_2 , \quad A_{32} = \gamma_2 ,$$

$$A_{41} = A_{31} + \beta_3 , \quad A_{42} = A_{32} + \gamma_3 - \beta_3 A_{31} , \quad A_{43} = -\beta_3 A_{32} ,$$

$$A_{51} = A_{41} + \beta_4 ,$$

$$A_{52} = A_{42} + \gamma_4 - \beta_4 A_{41} , \tag{4.2c}$$

$$A_{53} = A_{43} - \beta_4 A_{42} - \gamma_4 A_{31} ,$$

$$A_{54} = -\beta_4 A_{43} - \gamma_4 A_{32} , \quad \ldots .$$

We have worked out a considerable number of moments for the square lattice and the triangular lattice. The details of this work will be presented elsewhere, and only the results will be displayed here. For a square lattice, we have

$$m_2 = 4 ,$$

$$m_4 = 8 \cos(\phi) + 28 ,$$

$$m_6 = 24 \cos(2\phi) + 144 \cos(\phi) + 232 , \tag{4.3}$$

$$m_8 = 16 \cos(4\phi) + 96 \cos(3\phi)$$
$$+ 616 \cos(2\phi) + 2016 \cos(\phi) + 2156 ,$$

$$m_{10} = 40 \cos(6\phi) + 160 \cos(5\phi) + 840 \cos(4\phi)$$
$$+ 3120 \cos(3\phi) + 11\,080 \cos(2\phi)$$
$$+ 26\,320 \cos(\phi) + 21\,944 ,$$

where $\phi / 2\pi \Phi_0$ is the flux through a unit cell, and as is true for any even lattice, which has loops of only even number of sites, all the odd moments are zero. The Penrose lattice studied below is another example of an even lattice. It can also be shown that all the β parameters (diagonal elements) of the Lanczos matrix are zero in such a case. The first few nonzero matrix elements can be explicitly written as

$$\gamma_2 = z ,$$

$$\gamma_3 = \frac{1}{z} (m_4 - z^2) \tag{4.4}$$

$$\gamma_4 = \frac{1}{z^2 \gamma_3} (z m_6 - m_4^2) \cdots ,$$

where $z = m_2$ is the coordination number of the starting site. And the top eigenvalues of the first few approximants of the Lanczos Hamiltonian are explicitly given as

$$\epsilon_3 = \sqrt{z + \gamma_3} ,$$

$$\epsilon_4 = \left\{ \tfrac{1}{2} (z + \gamma_3 + \gamma_4) + \tfrac{1}{2} [(z + \gamma_3 + \gamma_4)^2 - 4 z \gamma_4]^{1/2} \right\}^{1/2} , \tag{4.5}$$

where ϵ_n corresponds to the nth order.

For a triangular lattice, we have

$$m_2 = 6 ,$$

$$m_3 = 12 \cos(\phi) ,$$

$$m_4 = 24 \cos(2\phi) + 66 ,$$

$$m_5 = 60 \cos(3\phi) + 300 \cos(\phi) , \tag{4.6}$$

$$m_6 = 12 \cos(6\phi) + 168 \cos(4\phi) + 840 \cos(2\phi) + 1020 ,$$

$$m_7 = 84 \cos(7\phi) + 504 \cos(5\phi)$$
$$+ 2604 \cos(3\phi) + 6888 \cos(\phi) ,$$

$$m_8 = 48 \cos(10\phi) + 432 \cos(8\phi) + 1968 \cos(6\phi)$$
$$+ 8568 \cos(4\phi) + 23\,904 \cos(2\phi) + 19\,890 ,$$

$$m_9 = 36 \cos(13\phi) + 432 \cos(11\phi) + 1980 \cos(9\phi)$$
$$+ 8496 \cos(7\phi) + 29\,628 \cos(5\phi) + 85\,944 \cos(3\phi)$$
$$+ 164\,124 \cos(\phi) ,$$

where $\phi / 2\pi \Phi_0$ is the flux through a triangular cell. Note that the even (odd) moments depend only on the even (odd) harmonics of the flux.

For the Penrose lattice with the starting site at the center of rotational symmetry, we have

$$m_2 = 5 ,$$

$$m_4 = 10 \cos(\phi) + 45 , \tag{4.7}$$

$$m_6 = 10 \cos(2\phi) + 10 \cos(\phi + 2\phi/\tau) + 20 \cos(\phi + \phi/\tau)$$
$$+ 190 \cos(\phi) + 20 \cos(\phi/\tau) + 435 ,$$

where $\phi / 2\pi \Phi_0$ is the flux through a fat cell. In this case, it is very difficult to carry out the moments to higher orders, but the first few moments will serve the purpose of demonstration below.

Using the moments given in Eqs. (4.3), (4.6), or (4.7), the Lanczos matrix elements (β and γ parameters) can be computed from Eqs. (4.2). In the following, we analyze how the first few approximations work for the phase diagrams and how the local geometries of the lattices affect the structures in them. The accurate computation of the

phase boundaries is not our major concern here.

First, consider the square lattice. In the inset of Fig. 1(a), the third through sixth orders of approximants of the phase diagram are shown. In general, this set of curves converge slower (although still monotonic) than those shown in the main part of this figure, the latter of which were computed using a uniform starting state. In the third order, the highest moment involved is m_4, which has field dependence contributions from paths circling a single cell. This gives rise to the dips at integral flux quanta but nowhere else. In the fourth order, the moment m_6 comes into play, which also has contributions from paths circling two-neighboring cells. This is responsible for the dip at half-flux quantum. In the fifth order, the curve tries to lower down near third and two-thirds flux quanta, as is expected from the field dependence of the moment m_8, but is not quite accomplished until the next order. Somehow the higher-order structures get depressed by the lower-order ones.

Second, consider the triangular lattice. Figure 8 shows the second through fifth-order approximants of the phase diagram. Unlike the square lattice case, the fine structures that appeared in lower-order approximants get shifted outwardly in the higher-order ones. Only the dips at $\frac{1}{2}$, $\frac{1}{4}$, and $\frac{3}{4}$ cell fluxes seem to get established in the highest-order shown. There seems to be a competition between the occurrence of phase coherence at different length scales. There are also some developing structures converging towards $\frac{1}{3}$ and $\frac{3}{8}$.

Finally, consider the Penrose lattice. In this case, the lack of translational symmetry prohibits the reduction to a one-dimensional problem and therefore the application

of the approach described in the last section. In Fig. 9(a), the experimental phase diagram is compared with our mean field result of a large size calculation. The correspondence is quite close. In Fig. 9(b), the third and fourth approximations of the phase diagram are shown. The third-order curve is a periodic function of the flux, which approximately locates the primary valleys and peaks. The periodicity is due to the fact that the only field dependence comes from the paths circling the fat tiles around the starting site in this order. The gross structure of the phase diagram is dominated by this periodic variation, because there are more fat tiles than the thin ones in the lattice. The approximation is improved in the fourth order by slightly shifting the locations and modulating the heights of the valleys and peaks. The result is a quasiperiodic function of the flux. Also note some fine structures that appear in this order. The roundings at the valleys are due to finite size effect.

For a nonregular lattice such as the Penrose lattice, different choice of the location of the starting state will produce different Lanczos Hamiltonians whose finite truncations will give inequivalent results, although they all approach the same limit as we increase the order of truncation. It is not clear which choice will give the most rapidly convergent series. For a macroscopically homo-

FIG. 8. $\Delta T_c(\Phi)$ vs magnetic flux per cell for a triangular lattice, computed from second- (top curve) through fourth-order truncations of the Lanczos Hamiltonian.
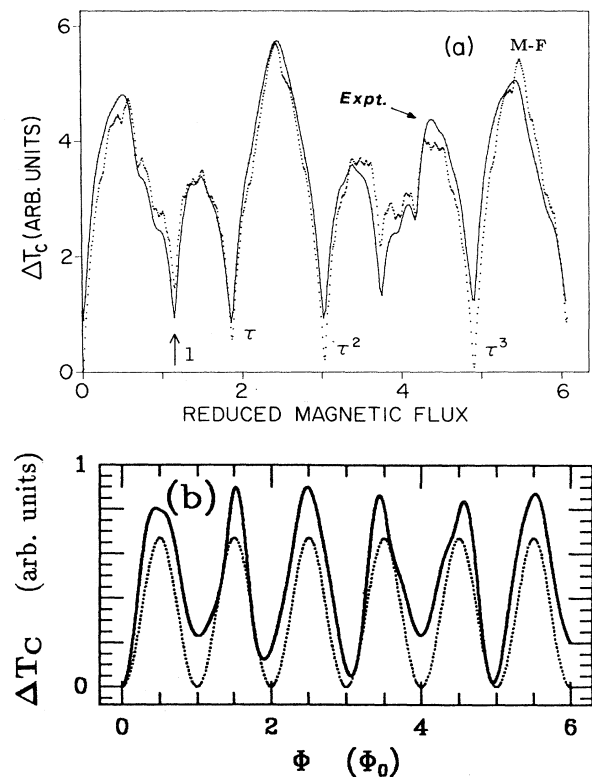
FIG. 9. Resistive transition temperature, ΔT_c, vs magnetic flux per large cell, for the Penrose lattice. (a) Mean-field phase diagram (dotted line) and the experimental data for the voltage (at a bias current of 8 μA) measured from a proximity-coupled array (Ref. 10). (b) Third- and fourth-order approximations to ΔT_c.

geneous system it might be more desirable to have an approximation scheme, with each stage exploring, on average, a different microscopic length scale.

V. CLUSTER MEAN-FIELD
AND RENORMALIZATION-GROUP THEORY

Mean-field theory has been one of the major theoretical tools in the study of phase transitions and critical phenomena. Because of its simplicity, the mean-field theory has been extensively used to study complex systems for which other approaches, such as the renormalization-group and Monte Carlo method, are often found formidably difficult. For superconducting networks in magnetic fields, where both inhomogeneity and frustration effects are present, it is only possible to study in great detail a few cases with simple geometries and at special field values. While the mean-field theory cannot predict precisely the type of phase transition and the critical exponents, it seems to be the only feasible approach to map out the phase diagram for a continuous range of the field and for a variety of network geometries.

An interesting question is why the mean-field phase diagrams reproduce so closely the experimental ones. There is some confusion on this issue, because one would expect that thermal fluctuations might invalidate the application of the mean field theory on a low-dimensional system (here 2D) near the critical region. To resolve this apparent paradox we suggest the following explanation. (1) The experimental data were not obtained in the very critical region. For instance, in the experiment of Behrooz et al.[9] the "critical temperature" data were taken with the condition that the network resistance drops to a fraction of its normal value immediately above the transition (about 2 mK above the real critical temperature). (2) Finite amount of current can destroy the criticality (e.g., see Springer and Van Harlingen[10]). (3) Although the mean-field transition temperature is generally higher than the true value, it still gives an approximately correct description of the cusplike and hierarchical structures that occur at commensurate cell fluxes of the phase diagram.

In order to get a concrete feeling about the effect of thermal fluctuations on the behavior of the phase diagram, we now present the result of a cluster mean-field (CMF) calculation for a square lattice of Josephson junctions. See Appendix B for details. We first mention how the standard mean-field (SMF) Eqs. (2.4) were derived. In the expression for $\langle e^{i\theta_i} \rangle$, the thermal average of the phase factor for the ith grain, one replaces, in the thermodynamic probability density, the variables $e^{i\theta_j}$ for all the other grains by their averages. The so obtained self-consistent equations are then linearized to yield (2.4). Now, in the CMF approach, $\langle e^{i\theta_i} \rangle$ is obtained by integrating out exactly the fluctuations of the ith grain and its nearest neighbors while replacing the other phase variables $e^{i\theta_k}$ by their averages. The linearized CMF equations are then solved for the transition temperature. In Figs. 10(a) and 10(b) the CMF phase diagram is compared with the SMF result. Because the local thermal fluctuations are taken into account in the CMF treat-
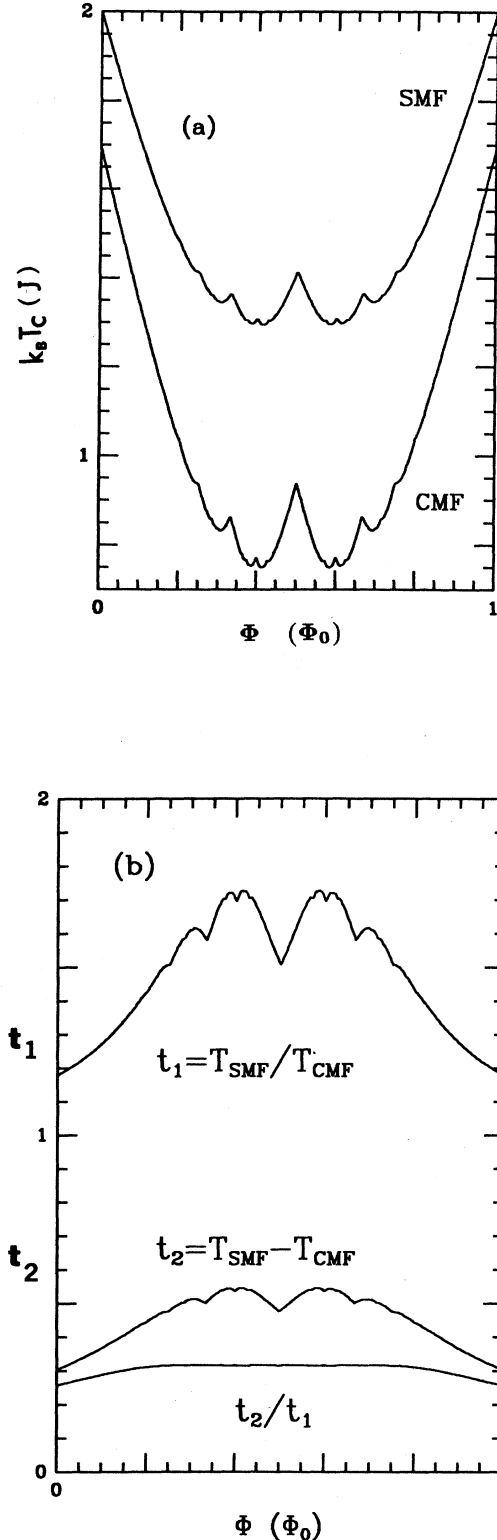
FIG. 10. (a) shows the predictions of the standard mean-field theory, top curve, and the cluster mean-field theory for the phase boundary of a Josephson-junction square array. Thermal fluctuations lower the transition temperature and make the peaks sharper. In (b), two curves shown in (a) are compared.

ment, the transition temperature gets lowered at every field value. Also note that the dips become sharper in the CMF phase diagram, but otherwise the two curves are strikingly similar in every detail. Our result is thus suggestive that thermal fluctuations merely make the hierarchical structures at commensurate fluxes more pronounced. To draw a firm conclusion on this, it would be very helpful to expand the cluster size beyond the nearest neighbors, but unfortunately this would require much more effort.

It is however relatively easier to devise an approximate renormalization-group theory by utilizing the information gained from our CMF approach. The basic idea is the following. We assumed that, under renormalization, only the couplings between nearest neighbors and next-nearest neighbors are present, and that they always have the same functional form

$$J_1\cos(\theta_i - \theta_j - A_{ij}), \quad J_2\cos(\theta_i - \theta_k - A_{ik}), \tag{5.1}$$

where (i,j) are nearest neighbors and (i,k) are next-nearest neighbors. The renormalized lattice is obtained by decimating every other site of the original lattice, so the unit cell doubles its area. The recursion relation between the coupling constants, (J_1, J_2) for the original and (J_1', J_2') for the new, is obtained by requiring that the linearized CMF equations for the original and the linearized SMF equations for the new be the same. The result is (see Appendix B)

$$J_1' = 2J_1 f(J_1)\cos(\phi/2) + 2J_2 ,$$

$$J_2' = J_1 f(J_1) , \tag{5.2}$$

$$\phi' = 2\phi ,$$

where ϕ and ϕ' are the fluxes through the unit cells, and $f(x) = I_1(x)/I_0(x)$ the ratio of two modified Bessel functions. If we use $z = \frac{1}{2}[1 - \cos(\phi/2)]$ in place of ϕ, the above recursive relations become

$$J_1' = 2J_1 f(J_1)(1 - 2z) + 2J_2 ,$$

$$J_2' = J_1 f(J_1) , \tag{5.3}$$

$$z' = 4z(1 - z) .$$

The mapping on z is independent of the other two variables and has the same form as the well studied logistic map[20] $x' = \lambda x(1 - x)$, with $\lambda = 4$. The flow of z is very chaotic in the sense that it has fixed cycles of all order corresponding to initial fractional fluxes, but that all these cycles are unstable. The flow of z disturbs the mapping on (J_1, J_2), causing a very exotic hierarchical behavior of the transition temperature as a function of the magnetic field (see below).

To obtain the critical temperature for a given initial flux, we run the mapping starting with $J_1 = J/kT$ and $J_2 = 0$. In general, J_1 and J_2 will either flow to infinity or zero together. With a critical initial value, they will flow to a fixed point, cycle for a fractional initial flux, or go into a seemingly chaotic path (confined in a finite region of the parameter space) for an irrational initial flux. The critical value of J/kT defines the transition temperature. The resulting phase diagram is plotted in Fig. 11. First,
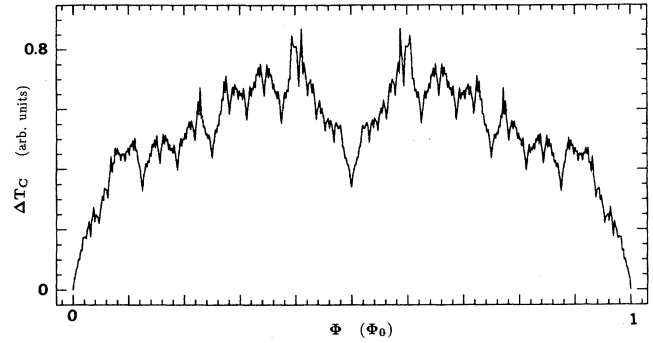
FIG. 11. Renormalization-group prediction for the phase boundary of a Josephson-junction square array. Note the pronounced hierarchical structure. The slopes at the dips are no longer finite (see the next figure). The suppression of peaks at fractional fluxes other than those with denominators of powers of 2 is an artifact of the approximation.

the general trend is the same as the mean-field result. Second, all the dips at $\phi = m/2^n$ (where m and n are integers) are enhanced, but those at other fractional fluxes are suppressed. We believe that this suppression is an artifact of the approximation made in our RG. The parameter space in our RG is too restrictive to take into consideration the fractional fluxes other than those $\phi = m/2^n$ for which the renormalization can bring to integers. Third, the transition temperature is nonzero everywhere, in contrast to the prediction of Teitel and Jayaprakash.[17] Finally, the dips are not only sharp, but also have infinite slopes. For example, the transition temperature near $\phi = 0$ behaves like

$$T_c(0) - T_c(0) \approx \phi^\alpha , \tag{5.4}$$

where $\alpha = 0.6605$. See Fig. 12.
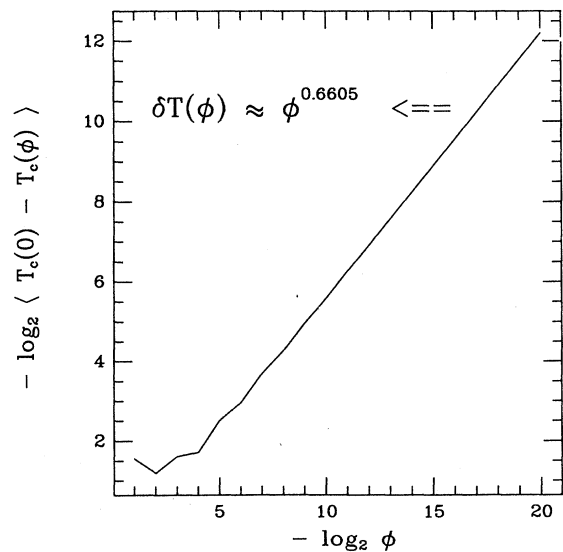
FIG. 12. A log-log plot of $\Delta T_c = T_c(0) - T_c(\Phi)$ near $\Phi = 0$. An exponent of 0.6605 is obtained from its slope, indicating an infinite slope in the linear plot.

VI. CONCLUSIONS

In this paper, we have studied the superconducting-normal phase boundaries of a variety of wire networks and Josephson-junction arrays in magnetic fields. We have computed mean-field phase diagrams for a number of geometries of the superconducting networks, and compared them with the corresponding experimental data. We have given a rather detailed analysis of the structures in the phase diagrams, and associated them with the geometrical properties of the networks. We have also studied the effect of thermal fluctuations by a cluster mean-field calculation and a real space renormalization-group theory.

Our introduction of the Lanczos method for the determination and analysis of the phase diagrams occupies a central position in this work. This method not only provides us a systematic approximation scheme for the phase diagrams, but also a rather powerful tool for a qualitative and quantitative analysis of the structures in them. As the order of approximation is increased, more and more geometrical information of the lattice is included in the treatment, and more and more fine structures are resolved. The correspondence is such that we can draw a number of specific conclusions regarding how the structures of various sizes are related to the geometries of the underlying lattices. The gross structure is determined by the statistical distribution of single-cell areas, disregarding their geometrical arrangement in the lattice. This explains why the Penrose, Fibonacci, and random Fibonacci lattices have phase diagrams of the same overall structure. The secondary dips or peaks are determined by the additional information about how the two- or three-neighboring cells are statistically correlated, but nothing more. In general, higher-order fine structures are due to correlations among the cells of larger clusters. The indexing of the dips in the phase diagrams can be easily read off from the periods of the Lanczos matrix elements. The sharpness of the dips is due to long-range correlations, and cannot be accounted for by local geometries. (The cusps present in small size systems are a different story, and they come from level crossings instead.) We are thus motivated to suggest an experiment on a set of lattices with a controlled degree of disorder in the geometrical arrangement of the cells, but without disorder in the cell areas. For instance, for the case of the Fibonacci lattice, the two extremes of the totally ordered and totally disordered have already been studied by Behrooz et al.[9] and in Sec. III of this paper. It would be interesting to examine the intermediate situations where the correlations among two or more neighboring cells of the ordered Fibonacci lattice are kept.

The effect of thermal fluctuations, which has not been taken into account by the standard mean-field theory, is also studied in this work. We have carried out a cluster mean-field calculation for a square array of Josephson junctions. In this treatment, the local fluctuations are included, and thereby should improve the result. It is found that the transition temperature is lowered and the dips become sharper. We have also devised a real space renormalization-group theory, which links the structures at fractional fluxes to those at integral ones, predicting a pronounced hierarchical behavior of the phase diagram. Furthermore, the dips not only get sharper but have infinite slopes, in contrast to the mean field prediction. We urge the experimentalists to check upon this issue by making measurements closer to criticality.

APPENDIX A

Here we consider how the nonlinear eigenvalue problem (2.5) can be reduced to a linear one. As we mentioned in the text, if $l_{ij}/\xi \ll 1$ at the critical temperature, then we can use Eq. (2.8) as an approximation. This is achieved by expanding the trigonometric functions in Eq. (2.5) to second order in l_{ij}/ξ followed by a change of variables for the wave functions. Now we examine through two examples to what extent the assumption $l_{ij}/\xi \ll 1$ is valid.

Consider first a square lattice with lattice constant l. Equation (2.5) now has the simple form

$$\cos\left[\frac{l}{\xi}\right]\phi_i = \frac{1}{4}\sum_j e^{iA_{ij}}\phi_j , \qquad (A1)$$

whose spectral edge, corresponding to the transition temperature, is bounded by the inequality $0 \leq \cos(l/\xi) < 0.65$, or equivalently $0 \leq l/\xi < 0.55\pi/2$, for the whole range of the flux. The approximation made in (2.8) is to replace $\cos(l/\xi)$ by $1 - l^2/2\xi^2$. Numerical evaluation of these two functions within the above bounds reveals a very small relative error (< 0.03), and therefore shows that the approximation is excellent for the purpose of determining the transition temperature.

Consider next a rectangular lattice with lattice constants l_x and l_y. Since the approximation is controlled by l_x/ξ and l_y/ξ, a reliable estimate of the degree of approximation can be achieved by considering the case of half-flux per cell, where the coherence length ξ is relatively

short. From Eq. (2.5) we have for half flux

$$\cot(x)\cot(y)=1 \ , \tag{A2}$$

where $x=l_x/\xi$ and $y=l_y/\xi$, while Eq. (2.8) gives

$$\frac{1-\frac{1}{2}x^2}{x}\frac{1-\frac{1}{2}y^2}{y}=1-\frac{1}{8}(x-y)^2 \ . \tag{A3}$$

The solutions of (A2) and (A3) for x are given respectively by

$$x=\frac{1}{1+r}\frac{\pi}{2} \ , \tag{A4}$$

and by

$$x=\left[\frac{2\{(1+r)^2-[(1+r)^4-2r(1+r^2)]^{1/2}\}}{r(1+r^2)}\right]^{1/2} \ , \tag{A5}$$

where $r=l_y/l_x$, and they are plotted for $0<r\leq1$ in Fig. 13 for comparison. It is seen that the two are very close even for large aspect ratio $r\approx0$. For a systematic study of the effect of anisotropy, see Hu and Chen.[21]

APPENDIX B

In this Appendix we present a somewhat detailed derivation of the SMF and CMF equations for a square lattice of Josephson junctions. In order to help the reader to follow the steps of our RG theory, we assume the presence of a next-nearest-neighbor coupling as well as a nearest-neighbor coupling of the form given in Eq.
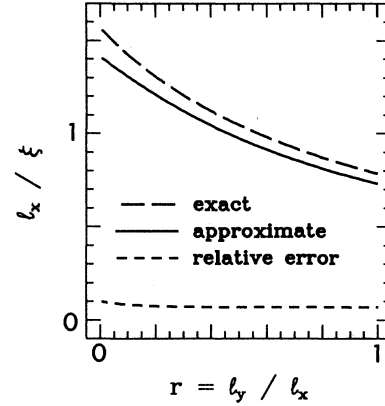
FIG. 13. Two solutions for $T_c(\Phi=\frac{1}{2})$ obtained from Eqs. (A2), exact, and (A3), approximate.

(5.1). For easier reference to the site labelings used below, we denote by i the site for which the phase variable, $e^{i\theta_i}$, is to be averaged, and denote by j, k, l, respectively, the nearest-, next-nearest, and third-nearest neighbors of site i. We will also denote by $\langle j,k\rangle$ those pairs of j and k sites who are nearest neighbors to each other, and similarly for $\langle j,l\rangle$. For illustration, see Fig. 14(a). Finally, the temperature will be absorbed into the coupling constants.

We first derive the SMF equation. For a fixed set of phase variables on the j and k sites, the average $\eta\equiv\langle e^{i\theta_i}\rangle$ is given by

$$\eta=\frac{\int e^{i\theta_i}\exp\left[J_1\sum_j\cos(\theta_i-\theta_j-A_{ij})\right]\exp\left[J_2\sum_k\cos(\theta_i-\theta_k-A_{ik})\right]}{\int\exp\left[J_1\sum_j\cos(\theta_i-\theta_j-A_{ij})\right]\exp\left[J_2\sum_k\cos(\theta_i-\theta_k-A_{ik})\right]} \ , \tag{B1}$$

where the integration is taken over the phase θ_i. The linearized SMF equations are obtained by replacing $e^{i\theta_j}$ and $e^{i\theta_k}$ with their averages $\eta_j=r_je^{i\phi_j}$ and $\eta_k=r_ke^{i\phi_k}$, and by expanding the right-hand side of the above equation to first order in r_j and r_k

$$\eta_i=J_1\sum_j r_j\int e^{i\theta_i}\cos(\theta_i-\phi_j-A_{ij})$$

$$+J_2\sum_k r_k\int e^{i\theta_i}\cos(\theta_i-\phi_k-A_{ik}) \ , \tag{B2}$$

or

$$\eta_i=\frac{J_1}{2}\sum_j\eta_je^{iA_{ij}}+\frac{J_2}{2}\sum_k\eta_ke^{iA_{ik}} \ , \tag{B3}$$

which is the same as Eq. (2.4) with $J_2=0$.

The derivation of the CMF equation is more involved

when the next-nearest-neighbor coupling is present. We first make use of a well known technique originally proposed by Migdal and Kadanoff in real-space renormalization-group theory.[22] The basic idea is to move a subset of bonds to some other places in the lattice in order to make the calculation tractable. This operation will certainly introduce some errors, but it turns out to be a quite good approximation for many statistical problems. We now apply this idea to our case and rotate a subset of next nearest bonds as shown in Fig. 14(b). We are then ready to derive the CMF equations.

For a given set of phase variables on the k and l sites, we have

$$\eta_i=\frac{\int e^{i\theta_i}\exp(S)}{\int\exp(S)} \ , \tag{B4}$$

where the integration is taken over θ_i and $\{\theta_j\}$, and
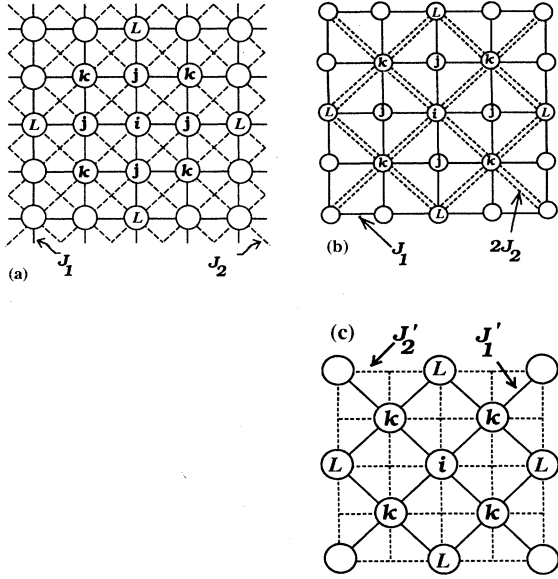
FIG. 14. Site labeling used in the cluster mean-field calculation and in the real-space decimation procedure for a Josephson-junction square array: (a) the original lattice, with the circles representing the superconducting grains; (b) a subset of next-nearest neighbor bonds in the original lattice has been rotated; (c) the renormalized lattice after decimating the j sites and every other site in the original lattice.

$$S = J_1 \sum_j \cos(\theta_i - \theta_j - A_{ij}) + J_1 \sum_{\langle j,k \rangle} \cos(\theta_j - \theta_k - A_{jk})$$
$$+ J_1 \sum_{\langle j,l \rangle} \cos(\theta_j - \theta_l - A_{jl})$$
$$+ 2J_2 \sum_k \cos(\theta_i - \theta_k - A_{ik}) . \tag{B5}$$

We then replace $e^{i\theta_k}$ and $e^{i\theta_l}$ with their averages, $\eta_k = r_k e^{i\phi_k}$ and $\eta_l = r_l e^{i\phi_l}$, and expand the right-hand side of Eq. (B4) to first order in r_k and r_l

$$\eta_i = \frac{\int S_1 e^{i\theta_i} \exp\left[J_1 \sum_j \cos(\theta_i - \theta_j - A_{ij}) \right]}{\int \exp\left[J_1 \sum_j \cos(\theta_i - \theta_j - A_{ij}) \right]} , \tag{B6}$$

where

$$S_1 = J_1 \sum_{\langle j,k \rangle} r_k \cos(\theta_j - \phi_k - A_{jk})$$
$$+ J_1 \sum_{\langle j,l \rangle} r_l \cos(\theta_j - \phi_l - A_{jl})$$
$$+ 2J_2 \sum_k r_k \cos(\theta_i - \phi_k - A_{ik}) . \tag{B7}$$

The integration can then be carried out by a simple change of variables $\theta_j \to \bar{\theta}_j = \theta_j - \theta_i + A_{ij}$, yielding

$$\eta_i = \frac{J_1}{2} f(J_1) \sum_{\langle j,k \rangle} \eta_k e^{i(A_{ij} + A_{jk})}$$
$$+ \frac{J_1}{2} f(J_1) \sum_{\langle j,l \rangle} \eta_l e^{i(A_{ij} + A_{jl})} + J_2 \sum_k \eta_k e^{iA_{ik}} , \tag{B8}$$

where $f(J_1)$ is the ratio of two modified Bessel functions

$$f(J_1) = \frac{\int d\theta \, e^{J_1 \cos(\theta)} e^{-i\theta}}{\int d\theta \, e^{J_1 \cos(\theta)}} = \frac{I_1(J_1)}{I_0(J_1)} . \tag{B9}$$

Now, for each k site there are two j sites entering the summation in the first term on the right-hand side of (B8), and the summation on j gives

$$\sum_{\langle j,k \rangle} \eta_k e^{i(A_{ij} + A_{jk})} = 2 \cos\left[\frac{\phi}{2} \right] \sum_k \eta_k e^{iA_{ik}} , \tag{B10}$$

assuming a cell flux of ϕ. In the second term on the right-hand side of (B8), there is only one j site for each l site in the summation, and we have

$$\sum_{\langle j,l \rangle} \eta_l e^{i(A_{ij} + A_{jl})} = \sum_l \eta_l e^{iA_{il}} . \tag{B11}$$

Finally we have

$$\eta_i = \left[J_1 f(J_1) \cos\left[\frac{\phi}{2} \right] + J_2 \right] \sum_k \eta_k e^{iA_{ik}}$$
$$+ \frac{J_1}{2} f(J_1) \sum_l \eta_l e^{iA_{il}} , \tag{B12}$$

which are our CMF equations. It should be noted that for our original Josephson-junction array the next-nearest-neighbor coupling is absent, therefore the bond rotation operation has no real effect as far as the CMF equations are concerned.

Our renormalization-group idea comes from the observation that the CMF equations (B12) have the same form as the SMF equations for an enlarged lattice [shown in Fig. 14(c) and obtained by decimating the j sites, and every other site, in the original lattice] with a cell flux twice as large as before, except for a change of coupling constants as given in Eq. (5.2). This set of equations provides the recursion relation needed to define a renormalization group.

---

[1]Throughout this paper, we will use the term *superconducting networks* referring to (i) thin-wire networks, (ii) proximity-effect junction arrays, and (iii) tunnel-junction arrays. For recent reviews see, for instance, B. Pannetier, J. Chaussy, and R. Rammal, Jpn. J. Appl. Phys. **26**, Suppl. 26-3, 1994 (1987); P. Martinoli, *ibid.*, **26**, Suppl. 26-3, 1989 (1987).

[2]B. Pannetier, J. Chaussy, and R. Rammal, J. Phys. (Paris) **44**, L853 (1983); B. Pannetier, J. Chaussy, R. Rammal, and J. Vil-

legier, Phys. Rev. Lett. **53**, 1845 (1984).

[3]D. J. Resnick, J. C. Garland, J. T. Boyd, S. Shoemaker, and R. S. Newrock, Phys. Rev. Lett. **47**, 1542 (1982); C. J. Lobb, D. W. Abraham, M. Tinkham, and T. M. Klapwijk, Phys. Rev. B **26**, 5268 (1982); C. J. Lobb, D. W. Abraham, and M. Tinkham, *ibid.* **27**, 150 (1983); D. Kimhi, F. Leyraz, and D. Ariosa, *ibid.* **29**, 1487 (1984); R. K. Brown and J. C. Garland, *ibid.* **33**, 7827 (1986); Ch. Leeman, Ph. Lerch, G.-A. Racine, and P. Martinoli, Phys. Rev. Lett. **56**, 1291 (1986).

[4]R. F. Voss and R. A. Webb, Phys. Rev. B **25**, 3446 (1982); R. A. Webb, R. F. Voss, G. Grinstein, and P. M. Horn, Phys. Rev. Lett. **51**, 690 (1983); M. Bushman, R. H. Cantor, J. M. Gordon, A. M. Goldman, and F. Yu, IEEE Trans. Magn. **MAG-23**, 1122 (1987); B. J. van Wees, H. S. J. van der Zant, and J. E. Mooij, Phys. Rev. B **35**, 7291 (1987).

[5]F. Nori and Q. Niu, Phys. Rev. B **37**, 2364 (1988); P. Santhanam, C. C. Chi, and W. W. Molzen, *ibid.* **37**, 2360 (1988).

[6]J. M. Gordon, A. M. Goldman, J. Maps, D. Costello, R. Tiberio, and B. Whitehead, Phys. Rev. Lett. **56**, 2280 (1986); B. Doucot, Y. Y. Wang, J. Chaussy, B. Pannetier, R. Rammal, A. Vareille, and D. Henry, *ibid.* **57**, 1235 (1986); H. J. Lee, M. G. Forrester, M. Tinkham, C. J. Lobb, Jpn. J. Appl. Phys. **26**, Suppl. 26-3, 1385 (1987); J. M. Gordon and A. M. Goldman, Phys. Rev. B **35**, 4909 (1987).

[7]J. M. Gordon, A. M. Goldman, and B. Whitehead, Phys. Rev. Lett. **59**, 2311 (1987); R. G. Steinmann and B. Pannetier, Europhys. Lett. **5**, 559 (1988); R. Rammal, T. Lubensky, and G. Toulouse, J. Phys. Lett. **44**, L65 (1983); J. Simonin and A. Lopez, Phys. Rev. Lett. **56**, 2649 (1986).

[8]E. Granato and J. M. Kosterlitz, Phys. Rev. B **33**, 6533 (1986); M. G. Forrester, H. J. Lee, M. Tinkham, and C. J. Lobb, *ibid.* **37**, 5966 (1988); S. P. Benz, M. G. Forrester, M. Tinkham, and C. J. Lobb (unpublished).

[9]A. Behrooz, M. Burns, H. Deckman, D. Levine, B. Whitehead,

and P. M. Chaikin, Phys. Rev. Lett. **57**, 368 (1986); Phys. Rev. B **35**, 8396 (1987).

[10]K. Springer and D. Van Harlingen, Phys. Rev. B **36**, 7273 (1987).

[11]Y. Y. Wang, R. Steinmann, J. Chaussy, R. Rammal, and B. Pannetier, Jpn. J. Appl. Phys. **26**, Suppl. 26-3, 1415 (1987).

[12]F. Nori, Q. Niu, E. Fradkin, and S. J. Chang, Phys. Rev. B **36**, 8338 (1987).

[13]M. Y. Choi, J. S. Cheung, and D. Stroud, Phys. Rev. B **35**, 1669 (1987); P. A. Kalugin, A. Yu. Kitaev, L. S. Levitov (unpublished).

[14]N. de Bruijn, Ned. Akad. Weten. Proc. Ser. A **43**, 27 (1981); **43**, 53 (1981); for studies of the 1D analog case see, for instance, F. Nori and J. P. Rodriguez, Phys. Rev. B **34**, 2207 (1986); Q. Niu and F. Nori, Phys. Rev. Lett. **57**, 2057 (1986).

[15]P. G. De Gennes, C. R. Acad. Sci. B **292**, 9 (1981); **292**, 279 (1981); S. Alexander, Phys. Rev. B **27**, 1541 (1983); R. Rammal, T. C. Lubensky, and G. Toulouse, *ibid.* **27**, 2820 (1983); H. J. Fink, A. López, and R. Maynard, *ibid.* **26**, 5237 (1982); J. M. Simonin, C. Wiecko, and A. López, *ibid.* **28**, 2497 (1983).

[16]W. Y. Shih and D. Stroud, Phys. Rev. B **28**, 6575 (1983); **30**, 6774 (1984); **32**, 158 (1985); D. Stroud and W. Y. Shih, Mater. Sci. Forum, **4**, 177 (1985).

[17]S. Teitel and C. Jayaprakash, Phys. Rev. Lett. **51**, 1999 (1983); Phys. Rev. B **27**, 598 (1983); T. C. Halsey, *ibid.* **31**, 5728 (1985); E. Granato and J. M. Kosterlitz, *ibid.* **33**, 4767 (1986).

[18]C. Paige, J. Inst. Math. Appl. **10**, 373 (1978).

[19]M. Floria (unpublished).

[20]See, for instance, H. G. Schuster, *Deterministic Chaos* (Physik-Verlag GbmH, Weinheim, 1984).

[21]C. R. Hu and R. L. Chen, Phys. Rev. B **37**, 7907 (1988).

[22]See, for instance, T. W. Burkhardt's article in *Real-Space Renormalization*, edited by T. W. Burkhardt and J. M. J. van Leeuwen (Springer-Verlag, Berlin, 1982).